https://doi.org/10.5194/egusphere-2026-6000
Preprint. Discussion started: 11 November 2026
© Author(s) 2026. CC BY 4.0 License.

Hysteresis metrics reveal land-use-dependent stormflow constituent dynamics in tropical Afromontane catchments

Zadoki Tabo[1,2], Suzanne R. Jacobs[1,2], Lutz Breuer[1,2]

[1]Institute for Landscape Ecology and Resources Management (ILR), Research Centre for BioSystems, Land Use and Nutrition (iFZ), Justus Liebig University Giessen, Heinrich-Buff-Ring 26, 35392 Giessen, Germany

[2]Centre for International Development and Environmental Research (ZEU), Justus Liebig University Giessen, Senckenbergstrasse 3, 35390 Giessen, Germany

Correspondence to: Zadoki Tabo (tabo.zadoki@umwelt.uni-giessen.de)

Abstract. High-frequency monitoring can resolve storm-event transport processes obscured by mean concentrations and low-frequency sampling, yet these dynamics remain poorly understood in tropical African headwaters. We analysed a six-year (2015–2020), 10-min record of rainfall, discharge, nitrate, dissolved organic carbon, electrical conductivity, and total suspended solids from natural forest, smallholder agriculture, and tea/tree plantation catchments in the South-West Mau, Kenya. Across 695 rainfall–runoff events, 2,506 event–constituent combinations were classifiable. Chemostasis dominated overall (70%), followed by mobilization (27%) and dilution (3%). Electrical conductivity (98%), nitrate (89%), and dissolved organic carbon (66%) were predominantly chemostatic, whereas total suspended solids were predominantly mobilized (69%). Of 1,472 responsive combinations, 1,323 yielded valid hysteresis geometry and 1,319 also had finite flushing index values for clustering. Joint analysis of the Lloyd hysteresis index, normalized loop area, and flushing index identified three stable response clusters of similar prevalence (33–34%): delayed flushing (Cluster 1: 33%), rapid mixed response (Cluster 2; 34%), and rapid flushing (Cluster 3; 33%).

Catchment–constituent setting strongly structured membership: Cluster 1 was dominated by dissolved organic carbon responses in natural forests and tea/tree plantations. Cluster 2 was characterized by dissolved constituents in smallholder agriculture and nitrate in the tea/tree plantation catchments. Finally, Cluster 3 was controlled by total suspended sediments, with highest occurrences in the natural forest and tea/tree plantation catchment. Antecedent dry period, discharge-peak count, and event rainfall differed among response groups, but their distributions overlapped substantially. Land use and constituent type therefore structured storm-event hysteresis and flushing responses more strongly than individual hydrological conditions.

1 Introduction

Stream water chemistry reflects catchment storage, source availability, hydrological connectivity, and biogeochemical processing, with the relative importance of these controls varying among individual hydrological events (Knapp et al., 2020; Musolff et al., 2021). Rainfall can activate previously weakly connected hillslope, riparian, soil, and channel sources, thereby changing the pathways and timing of constituent export (Bracken et al., 2013; Bujak-Ozga et al., 2025). Concentration–

https://doi.org/10.5194/egusphere-2026-6000
Preprint. Discussion started: 11 November 2026
© Author(s) 2026. CC BY 4.0 License.

discharge (C–Q) relationships characterize how concentrations of solute and particulate constituents respond to changing flow: increasing concentrations indicate mobilization, decreasing concentrations indicate dilution or source limitation, and near-constant concentrations indicate chemostatic behaviour (Godsey et al., 2009; Knapp et al., 2020). However, long-term or aggregated C–Q relationships can obscure substantial event-to-event variation, making high-frequency measurements necessary to resolve storm-scale source activation and transport (Knapp et al., 2020; Musolff et al., 2021; Delesantro et al., 2024). Event-scale hysteresis further resolves concentration trajectories relative to discharge: clockwise loops indicate the mobilisation of nearby sources of solutes and solids, anticlockwise loops suggest rapid dilution or the mobilisation of distal sources and slower transport, and figure-8/mixed trajectories represent complex responses with activation of multiple sources and flow paths; these geometries can support source-timing hypotheses but do not uniquely identify source or pathway (Evans and Davies, 1998; Butturini et al., 2008; Mazilamani et al., 2024). Quantitative hysteresis metrics and transparent event delineation are important because inferred loop characteristics can depend on how storm events and trajectories are defined (Liu et al., 2021).

High-frequency monitoring is essential for resolving intrastorm hydrochemical trajectories because sub-hourly observations capture rapid concentration changes, source activation, and pathway switching that are easily obscured by lower-frequency sampling (Knapp et al., 2020; Musolff et al., 2021; Delesantro et al., 2024). This temporal resolution is particularly important in headwater catchments, where rainfall can rapidly expand hydrological connectivity and generate short-lived but substantial solute and sediment pulses (Bujak-Ozga et al., 2025). These responses are strongly constituent-specific. Storm-event nitrate (NO_3–N) dynamics often reflect rapid mobilization from shallow or newly connected sources, with the timing and magnitude of export controlled by source availability, antecedent conditions, and evolving flow pathways (Vaughan et al., 2017; Husic et al., 2023; Wang et al., 2024). In the South-West Mau, high-frequency observations similarly show that land use modifies nitrate concentrations and event-scale routing between forested and managed catchments (Jacobs et al., 2018b). Dissolved organic carbon (DOC) responses are likewise governed by transient hydrological connection of organic-rich soil, riparian, and other stored carbon sources, producing strong event-to-event variation in concentration and hysteresis behaviour (Vaughan et al., 2017; Delesantro et al., 2024; Bujak-Ozga et al., 2025). In contrast, electrical conductivity (EC) commonly reflects mineralized pre-event or groundwater contributions and often declines during stormflow as lower-conductivity event water dilutes these sources (Bücker et al., 2011; Knapp et al., 2020), whereas total suspended sediments (TSS) respond strongly to high rainfall, sediment availability, erosion, and channel or hillslope remobilization (Stenfert Kroese et al., 2020; Long et al., 2024; Jing et al., 2025; Kim et al., 2026). Despite increasing use of high-frequency monitoring, long-term multi-constituent studies that integrate response prevalence, hysteresis geometry, flushing magnitude, and hydrometeorological controls remain uncommon, particularly in tropical montane catchments (Mazilamani et al., 2024).

Land use conversion can reorganize source availability and hydrological connectivity by altering infiltration, flow paths, nutrient inputs, and sediment supply. In the South-West Mau specifically, forest, smallholder agriculture, and tea/tree plantation catchments differ in hydrological pathways, nutrient export, high-frequency nitrate behaviour, and sediment supply (Jacobs et al., 2018a, 2018b; Stenfert Kroese et al., 2020), shifting hysteresis direction, loop complexity, and mobilization

https://doi.org/10.5194/egusphere-2026-6000
Preprint. Discussion started: 11 November 2026
© Author(s) 2026. CC BY 4.0 License.

thresholds (Lintern et al., 2018; Vaughan et al., 2017). Yet event-scale mechanisms remain poorly documented in tropical African montane headwaters, and multi-constituent studies integrating response prevalence, hysteresis geometry, flushing magnitude, and nonlinear controls are rare (Mazilamani et al., 2024). Kenya's Mau Forest Complex, an Afromontane water tower, provides an ideal gradient to study these contrasts (Krhoda, 1988; Jacobs et al., 2018a). Although previous studies have shown that land use alters seasonal hydrochemistry and sediment loads in this region (Jacobs et al., 2018b; Stenfert Kroese et al., 2020), event-scale mechanisms, loop geometries, and hydrometeorological drivers remain unresolved. To separate complementary dimensions of stormflow behaviour, the Lloyd hysteresis index (HI_{Lloyd}) quantifies loop direction (clockwise vs. anti-clockwise), normalized loop area (A_{loop}) measures geometric separation between the two limbs as indicator for constituent response timing, and the Vaughan et al. (2017) flushing index (FI) measures the direction of change in concentration from event onset to the peak-discharge to infer on mobilisation or dilution of the constituent (Lloyd et al., 2016b; Vaughan et al., 2017; Zuecco et al., 2016). Treating HI_{Lloyd}, A_{loop} and FI jointly allows loop direction, response timing, and flushing behaviour to be interpreted as complementary evidence, and reduces reliance on any single metric as a unique indicator of source or flow path.

Using a six-year (2015–2020), 10-min record from three headwater catchments in the South-West Mau, we examine storm-event dynamics of NO_3^-, DOC, EC, and TSS across a land-use gradient comprising natural forest, smallholder agriculture, and commercial tea/tree plantations. The study aims to: (1) characterize hydrochemical regimes, constituent-response prevalence, and event-level chemical status (chemostasis, mobilization, or dilution) across the contrasting catchments; (2) quantify complementary dimensions of event-scale transport using loop type, the Lloyd hysteresis index (HI_{Lloyd}), normalized loop area (A_{loop}), and flushing index (FI) and identify recurrent multivariate response patterns from their joint behaviour; and (3) evaluate how these individual and multivariate responses vary with catchment–constituent setting, rainfall–runoff structure, storm forcing, and antecedent hydrological and chemical conditions. NO_3–N, DOC, and TSS form the primary multi-constituent comparison, whereas EC is retained as a conservative reference and interpreted cautiously because its responsive sample was smaller and uneven among catchments. Separating response prevalence, chemical status, response timing, rising and falling-limb separation, within-event trajectory structure, and flushing magnitude enabled plausible source-activation, pathway-switching, and transport mechanisms to be evaluated without treating any individual metric as a unique indicator of source or flow path.

2 Materials and methods

2.1 Study area

The South-West Mau study area lies at approximately 1,700–2,700 m a.s.l. within a humid tropical montane headwater system that sustains perennial downstream flow. The three monitored catchments represent a land-use gradient from natural forest (NF) to smallholder agriculture (SHA), and tea and tree plantations (TTP) (Fig. 1).

https://doi.org/10.5194/egusphere-2026-6000
Preprint. Discussion started: 11 November 2026
© Author(s) 2026. CC BY 4.0 License.

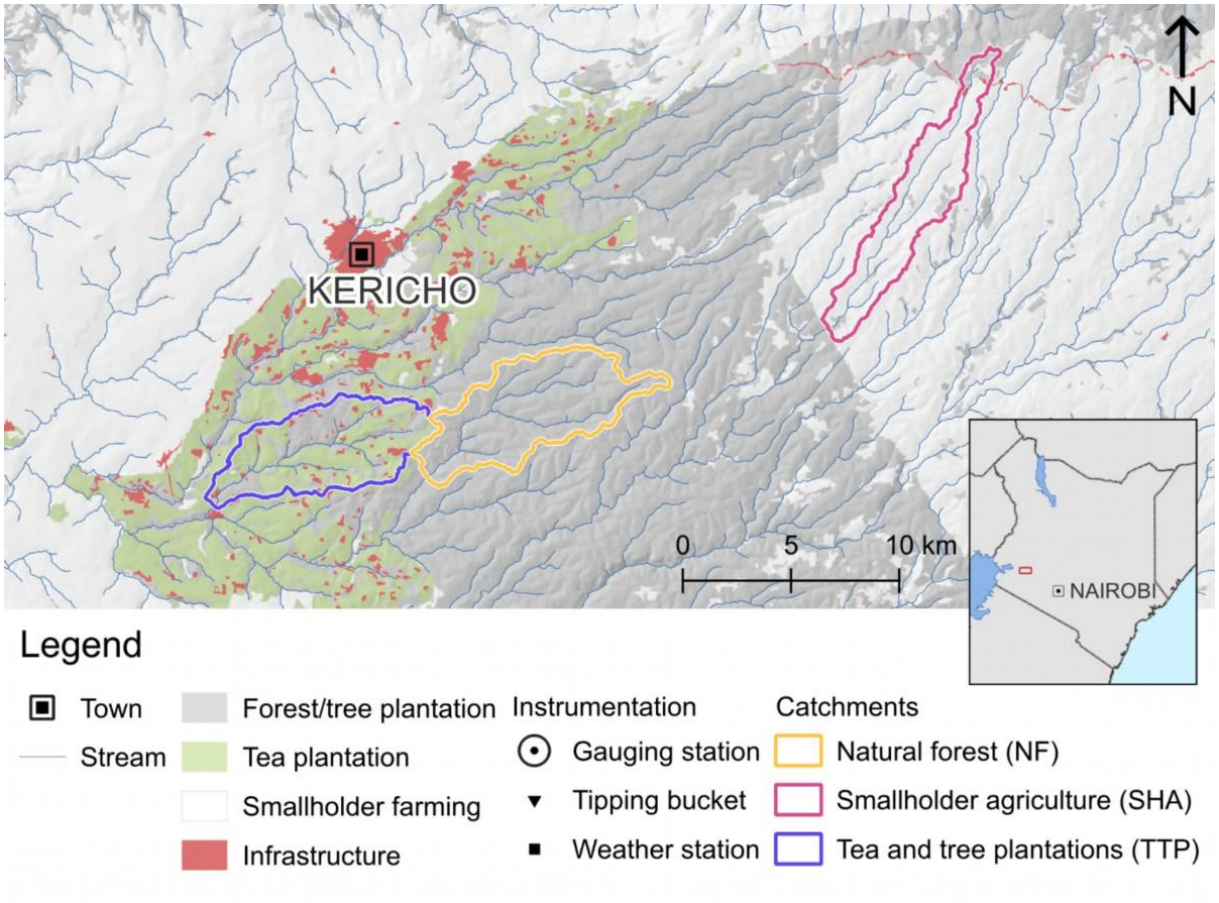


Figure 1. Location of the three study catchments in the South-West Mau region, Kenya: natural forest (NF), smallholder agriculture (SHA), and tea and tree plantations (TTP). Catchment boundaries, stream networks, major land-cover classes, nearby towns, and the locations of gauging stations, tipping-bucket rain gauges, and weather stations are shown. The inset indicates the location of the study area within Kenya. Land-use information was derived from Swart (2016), while stream networks and catchment boundaries were derived from the NASA Shuttle Radar Topography Mission (SRTM) 30 m digital elevation model (NASA JPL, 2013).

The geology is dominated by early Miocene volcanic rocks, with phonolites mainly at lower elevations and phonolitic nephelinites becoming more common upslope (Binge, 1962; Jacobs et al., 2018b). Soils are deep, strongly weathered, and highly leached, with humic Nitisols dominating most of the area and mollic Andosols occurring locally in the eastern sector (Krhoda, 1988). These deep volcanic soil and weathering profiles provide substantial subsurface storage that supports perennial flow and influences stormflow routing (Jacobs et al., 2018a). The climate is humid with bimodal rainfall, with long rains mainly from April to August, short rains from October to December, and the driest period generally in January–February. Mean annual precipitation is approximately 1,800–1,980 mm, mean annual temperature is about 16°C at 2,000 m a.s.l., and potential evapotranspiration averages about 1,570 mm yr^{-1}, generally decreasing with increasing elevation (Krhoda, 1988; Edwards and Blackie, 1981). Forest margins bordering smallholder communities are affected by cattle grazing, fuel-wood

https://doi.org/10.5194/egusphere-2026-6000
Preprint. Discussion started: 11 November 2026
© Author(s) 2026. CC BY 4.0 License.

extraction, illegal timber logging, and localized charcoal production (Brandt et al., 2018). The monitored catchments therefore provide land-use contrast for assessing stormflow generation, C–Q hysteresis, and export of NO_3–N, DOC, EC, and TSS.

2.2 Monitoring infrastructure and data quality

Precipitation, stream stage, and water quality parameters were monitored at 10-min intervals from January 2015 to December 2020. NO3-N, DOC and turbidity were recorded with a UV/Vis spectrometer probe (spectro::lyser, s::can Messtechnik GmbH, Austria) and electrical conductivity with a 4-electrode direct-contact sensor (condu::lyser, s:.can Messtechnik GmbH, Austria). Sensor records were checked against calibration records, manual samples, and field observations. Stream stage was recorded with a radar-based sensor (VEGAPULS WL61, VEGA Grieshaber KG, Germany) and was converted to discharge using site-specific rating curves (Jacobs et al., 2018a), and TSS was estimated from turbidity using the calibration developed by Stenfert Kroese et al. (2020). Physically impossible negative discharge or constituent values were treated as missing. The hydrological year ran from October to September. Before event delineation, discharge and constituent series were smoothed using a centred ±20-min moving average to reduce short-term measurement variability.

2.3 Delineation of rainfall-runoff events

Because hydrograph response and recession differed among catchments, event-separation criteria were site specific. Rainfall events were identified using a minimum accumulated depth of 1 mm and catchment-specific inter-event dry gaps (t_{Dry}) of 2 h in NF and SHA and 3 h in TTP. The longer TTP gap reflected its slower hydrographical response while limiting overlap between successive rainfall events.

Candidate rainfall events were linked to discharge responses when hydrograph rise began within 6 h of rainfall onset. The response-search window extended for up to 72 h or until the onset of the next independently delineated rainfall event, whichever occurred first. Multiple rainfall pulses within the same delineated event were retained, whereas runoff responses overlapping separate preceding or subsequent events were excluded. A measurable runoff response required a peak-flow ratio $R_Q = Q_p/Q_0$ of at least 1.20 in NF and TTP and 1.15 in SHA, where Q_p is peak discharge and Q_0 is discharge at event onset. Hydrological independence was additionally assessed using an antecedent dry period (t_{ADP}) of at least 10 h in NF and TTP and 8 h in SHA. Hydrograph recovery was quantified as $R_{end} = (Q_{end} - Q_0)/(Q_p - Q_0)$, where Q_{end} is discharge at the end of the response window; accepted events required $R_{end} \leq 0.10$ in NF and SHA and $R_{end} \leq 0.15$ in TTP. The higher TTP limit accommodated its slower recession while limiting overlap between successive events. These site-specific response thresholds accommodated observed differences in response magnitude and recession behaviour while preserving hydrological independence among accepted events.

2.4 Event-scale metrics

For each accepted event, we calculated rainfall, discharge, antecedent-state, runoff-partitioning, and hydrochemical descriptors. Rainfall metrics included event depth, duration, maximum and mean intensity, antecedent dry period, precipitation totals over the preceding 1, 3, 5, 7, 15, and 21 days, and a 21-day exponentially weighted antecedent precipitation index (Eq. 1).

https://doi.org/10.5194/egusphere-2026-6000
Preprint. Discussion started: 11 November 2026
© Author(s) 2026. CC BY 4.0 License.

$$API_{21}(t_0) = \sum_{d=1}^{21} k^{d-1} P_d \quad (1)$$

Where t_0 is the event onset time, P_d is precipitation during the d-th 24-h period preceding event onset and $k = 0.85$ is the daily decay coefficient (Hong et al., 2007).

Hydrological metrics included initial, peak, final, and mean discharge; rising- and falling-limb durations; response delay; relative lag; peak amplification; discharge volume; direct-runoff volume and depth; runoff coefficient; and baseflow contribution. Antecedent discharge was summarized over 3, 7, and 30 days. Constituent metrics included pre-event baseline (C_0), minimum, maximum, mean, and flow-weighted concentrations, change from baseline and event load. Loads were calculated from discharge and concentration at 10-min time steps. Within-event time-step data were summaries using valid counts and the relevant minima, maxima, means, medians, standard deviations, interquartile ranges, and coefficients of variation.

Flow regimes were defined separately for each catchment from the 33rd and 66th percentiles of the complete six-year daily mean discharge record. Event-onset discharge (Q_0) was classified as low flow at or below the 33rd percentile, mid flow above the 33rd and at or below the 66th percentile, and high flow above the 66th percentile. Using the long-term discharge distribution prevented the selected storm sample from defining specific flow classes and allowed event responses to be interpreted against catchment-specific storage and connectivity conditions (Bracken et al., 2013; Jacobs et al., 2018a).

Chemical status was evaluated at each valid 10-min timestep using event-specific baseline concentrations (C_0) and a ±15% concentration change threshold (Butturini et al., 2006). For concentration C_t at timestep t, the instantaneous chemical status (S_t) was defined as given in Eq. (2). A single event-level chemical status was then assigned to each event–constituent combination as the category occurring during the greatest number of valid timesteps within the event. In cases where two or more categories had equal counts, ties were resolved in the order chemostasis, mobilization, and dilution. Consequently, an event–constituent combination could show a response to rainfall because of a brief excursion beyond the ±15% baseline band while remaining event-level chemostatic when most valid timesteps occurred within the band.

$$S_t = \begin{cases} \text{mobilization}, & C_t > C_0(1 + 0.15) \\ \text{dilution}, & C_t < C_0(1 - 0.15) \\ \text{chemostasis}, & C_0(1 - 0.15) \le C_t \le C_0(1 + 0.15) \end{cases} \quad (2)$$

Event analyses used three nested populations: (1) the classifiable population had sufficient concentration data for event-level status (Section 2.4.1); (2) the responsive population additionally contained at least one excursion beyond ±15% of C_0 (Section 2.4.1); (3) and the geometry-resolved population additionally had finite HI_{Lloyd}, finite A_{loop}, and a valid loop class (Section 2.4.2). Because each hydrological event was evaluated for each constituent, one event could contribute several event–constituent combinations; changing denominators therefore reflect inclusion criteria, not different status rules.

2.4.1 Baseline-based constituent response and recovery

Constituent response and recovery were evaluated independently for each event–constituent combination. Combinations were retained when valid concentration observations covered at least 90% of the event window. The pre-event baseline concentration

https://doi.org/10.5194/egusphere-2026-6000
Preprint. Discussion started: 11 November 2026
© Author(s) 2026. CC BY 4.0 License.

($\boldsymbol{C_0}$) was defined as the median valid concentration observed from six to two timesteps (i.e. 1 hour to 20 minutes) before hydrograph rise, thereby providing a local pre-event reference while minimizing potential early event-related concentration changes; however, residual influence from recession of preceding events could not be excluded. An event–constituent combination was classified as responsive when its maximum relative deviation from $\boldsymbol{C_0}$ during the event was at least 15% (Eq. 3):

$$max\left(\frac{|C_t - C_0|}{|C_0|}\right) \geq 0.15 \quad (3)$$

where C_t is the concentration at timestep t. The 15% criterion was applied consistently across constituents as a study-specific operational threshold to distinguish measurable event-related excursions from short-term variability around the pre-event baseline. Similar to hydrograph recovery, signal recovery at the end of the event window was quantified using R_{rec} (Eq. 4).

$$R_{\text{rec}} = \frac{|\, C_{\text{end}} - C_0 \,|}{|\, C_{\text{peak}} - C_0 \,|} \quad (4)$$

where C_{end} is the final valid concentration within the event window and C_{peak} is the concentration showing the greatest absolute deviation from C_0. An event–constituent combination was classified as recovered when $R_{\text{rec}} \leq 0.20$.

2.4.2 Hysteresis metrics and loop classification

Hysteresis metrics were computed for responsive event–constituent combinations with at least 10 paired discharge–concentration observations and at least four distinct observations on each hydrograph limb. Within each event, discharge and concentration were normalized to the interval 0–1 using their event-specific extrema (Eq. 5).

$$\phi_{\text{norm}} = \frac{\phi - \phi_{\text{min}}}{\phi_{\text{max}} - \phi_{\text{min}}} \epsilon\, (0,1) \quad (5)$$

where $\phi \epsilon \{Q, C\}$. Following Lloyd et al. (2016b), normalized rising- and falling-limb concentrations were linearly interpolated at m=19 discharge-grid positions (k=0.05, 0.10, …, 0.95). The grid-specific hysteresis index HI_{k} was the difference in concentration on the rising limb minus that on the falling limb (Eq. 6): positive values indicate clockwise loops or earlier delivery and negative values anticlockwise loops or delayed delivery. HI_{Lloyd} was the mean signed difference across the grid (Eq. 7), whereas A_{loop} was the absolute area between the two limbs (Eq. 8) and therefore quantified limb separation independently of direction (Zuecco et al., 2016). Separately, the flushing index (FI; Vaughan et al., 2017) was calculated using Eq. (9), where $C_{norm,\text{initial}}$ was the first finite normalised concentration within the accepted event window, and $C_{norm,Q_{peak}}$ was observed normalised concentration at the peak-discharge timestep. FI is bounded from -1 to +1; positive values indicate enrichment at peak discharge relative to event onset and negative values indicate depletion. When concentration was missing at the exact peak-discharge timestep, FI was treated as missing rather than interpolated.

$$HI_k = C_{norm,\text{rise}}(Q_k) - C_{norm,\text{fall}}(Q_k) \quad (6)$$

$$HI_{\text{Lloyd}} = \frac{1}{m} \sum_{k=1}^{m=19} H\, I_k \quad (7)$$

https://doi.org/10.5194/egusphere-2026-6000
Preprint. Discussion started: 11 November 2026
© Author(s) 2026. CC BY 4.0 License.

$$A_{\text{loop}} = \int_0^1 \left| C_{n,\text{rise}}(q) - C_{n,\text{fall}}(q) \right| \, dq \tag{8}$$

$$\text{FI} = C_{norm,Q_{peak}} - C_{norm,\text{initial}} \tag{9}$$

Events were assigned to five mutually exclusive operational loop types according to the sign, magnitude and zero crossings of HI_{k} across the normalized discharge grid. This operational classification follows the broader event-scale hysteresis framework reviewed by Liu et al. (2021). Direct or synchronous responses were assigned when the overall loop magnitude was negligible, defined as mean($|HI_k|$)<0.02. Pure clockwise loops were classified when $HI_k \geq -0.01$ at all grid points and mean($|HI_k|$) ≥ 0.02. While a pure clockwise loop should have values exclusively above zero the small negative value for HI_{k} provides a tolerance for minor deviations. Pure anticlockwise loops were classified when $HI_k \leq 0.01$ at all grid points, again allowing for minor deviations, and mean($|HI_k|$) ≥ 0.02. Single-line-plus-loop events were identified when $|HI_k| < 0.01$ over the lower-flow range ($k \leq 0.30$), followed by divergence into a distinct unidirectional loop at higher flows ($k > 0.30$), following the same criteria as for pure clockwise and anticlockwise loops. Figure-8 or mixed loops were assigned when HI_{k} included at least one value $> +0.01$ and one value < -0.01 within the core discharge grid($0.10 \leq k \leq 0.90$), indicating shifts in the relative timing of concentration and discharge across flow stages (Vaughan et al., 2017). Combinations with non-finite HI_{Lloyd} or A_{loop} values, insufficient variation on either limb, a zero-normalization range, or no valid operational loop class were excluded from the geometry-resolved population. Cases with missing FI were retained for the hysteresis analysis but excluded from the clustering, which required finite HI_{Lloyd}, A_{loop}, and FI.

2.5 Multivariate response clustering and environmental associations

The analysis was designed to cluster event–constituent combinations that showed similar joint patterns of loop direction and complexity, response timing, and flushing behaviour. The clustering subset comprised 1,319 of the 1,323 responsive, geometry-resolved combinations for which HI_{Lloyd}, A_{loop}, and FI were all finite. Each metric was Winsorized at the 1st and 99th percentiles and converted to a robust Z-score using the sample median and median absolute deviation scaled by 1.4826 (Rousseeuw and Croux, 1993; Leys et al., 2013). Euclidean distances were then calculated between all combinations so that observations with similar timing, loop direction, and flushing magnitude were positioned close together in the multivariate response space.

These distances were grouped using partitioning around medoids, which assigns observations to clusters around an actual representative observation, or medoid (Kaufman and Rousseeuw, 1990). Candidate solutions with $k = 2 - 6$ were compared and the selected solution maximized average silhouette width while requiring every cluster to contain at least 5% of observations and 20 records. Silhouette width measured how clearly an observation fitted its assigned cluster relative to the alternatives, whereas bootstrap–Jaccard similarity measured whether comparable memberships reappeared in 200 resampled datasets (Hennig, 2007). Silhouette distributions, Jaccard similarities, and partitioning around medoids were retained as diagnostics, and clusters were interpreted as reproducible response regions rather than discrete mechanistic classes.

https://doi.org/10.5194/egusphere-2026-6000
Preprint. Discussion started: 11 November 2026
© Author(s) 2026. CC BY 4.0 License.

After the response clusters were identified, we tested whether catchments, constituents, catchment–constituent combinations, loop types, and hydrograph features occurred more or less often than expected within each cluster (Musolff et al., 2021). Pearson χ^2 tests with 5,000 Monte Carlo replicates tested whether these categories were distributed differently among response clusters; p-values were adjusted using the Benjamini–Hochberg false-discovery-rate procedure at $\alpha = 0.05$ (Benjamini and Hochberg, 1995). Adjusted standardized residuals and observed-to-expected ratios identified overrepresented or underrepresented combinations, meaning combinations that occurred more or less often than expected from the overall table, not higher or lower concentrations. Positive overrepresentation required a residual ≥ 2 and an observed-to-expected ratio > 1. Discharge peaks were detected after five-point moving-median smoothing and required prominence $\geq 10\%$ of the event discharge range and separation ≥ 2 h. Predefined candidate hydrological variables (event rainfall, rainfall duration, maximum and mean rainfall intensity, antecedent dry period, initial discharge, discharge-peak count, and discharge-peak separation) were compared among response clusters using Kruskal–Wallis tests followed, when significant, by Benjamini–Hochberg-adjusted pairwise Wilcoxon tests (Benjamini and Hochberg, 1995).

To assess how hydrological conditions were associated with the probability of response-cluster membership, one-versus-rest binomial models were fitted separately for each cluster. Hydrological variables showing significant differences among clusters in the preceding screening analysis were used as predictors. Continuous predictors were represented by thin-plate regression splines with $k = 5$, whereas discrete count variables were fitted as categorical effects. Separate models were fitted for each response group and included catchment–constituent combination as an adjustment factor to account for unequal representation among clusters. Models used restricted maximum likelihood and required at least 100 finite observations, adequate predictor variation, and both outcome classes. Adjusted probabilities were averaged over the observed catchment–constituent distribution and reported with pointwise 95% confidence intervals. For continuous predictors, the transition point was defined by the greatest absolute first derivative, and the transition range comprised contiguous values where the derivative remained at least 50% of its maximum. These ranges were interpreted as sample-dependent probability transitions rather than deterministic or causal thresholds.

3 Results and discussion

3.1 Stormflow hydrochemical regime shifts

The continuous 2015–2020 record established distinct hydrological and hydrochemical baselines among the three catchments (Fig. 2; Table 1). Mean discharge was highest in NF (0.84 $m^3 s^{-1}$), followed by TTP (0.71 $m^3 s^{-1}$) and SHA (0.52 $m^3 s^{-1}$). Mean NO_3–N concentrations increased across the land-use gradient from 0.38 mg N L^{-1} in NF to 1.74 mg N L^{-1} in TTP. Mean DOC concentrations varied less among catchments (2.13–2.91 mg L^{-1}), but maxima were substantially higher in SHA and TTP (about 24 mg L^{-1}) than in NF (8.6 mg L^{-1}). TSS showed the strongest absolute land-use contrast, mean concentrations were 31.7 mg L^{-1} in NF, 120 mg L^{-1} in SHA, and 43.9 mg L^{-1} in TTP, with maxima of 1,266, 3,358 mg L^{-1} and 2,848 mg L^{-1}, respectively. EC differed in mean concentration among sites but showed comparatively low relative variability over the full record (CV=8.6–25.0%).

https://doi.org/10.5194/egusphere-2026-6000
Preprint. Discussion started: 11 November 2026
© Author(s) 2026. CC BY 4.0 License.

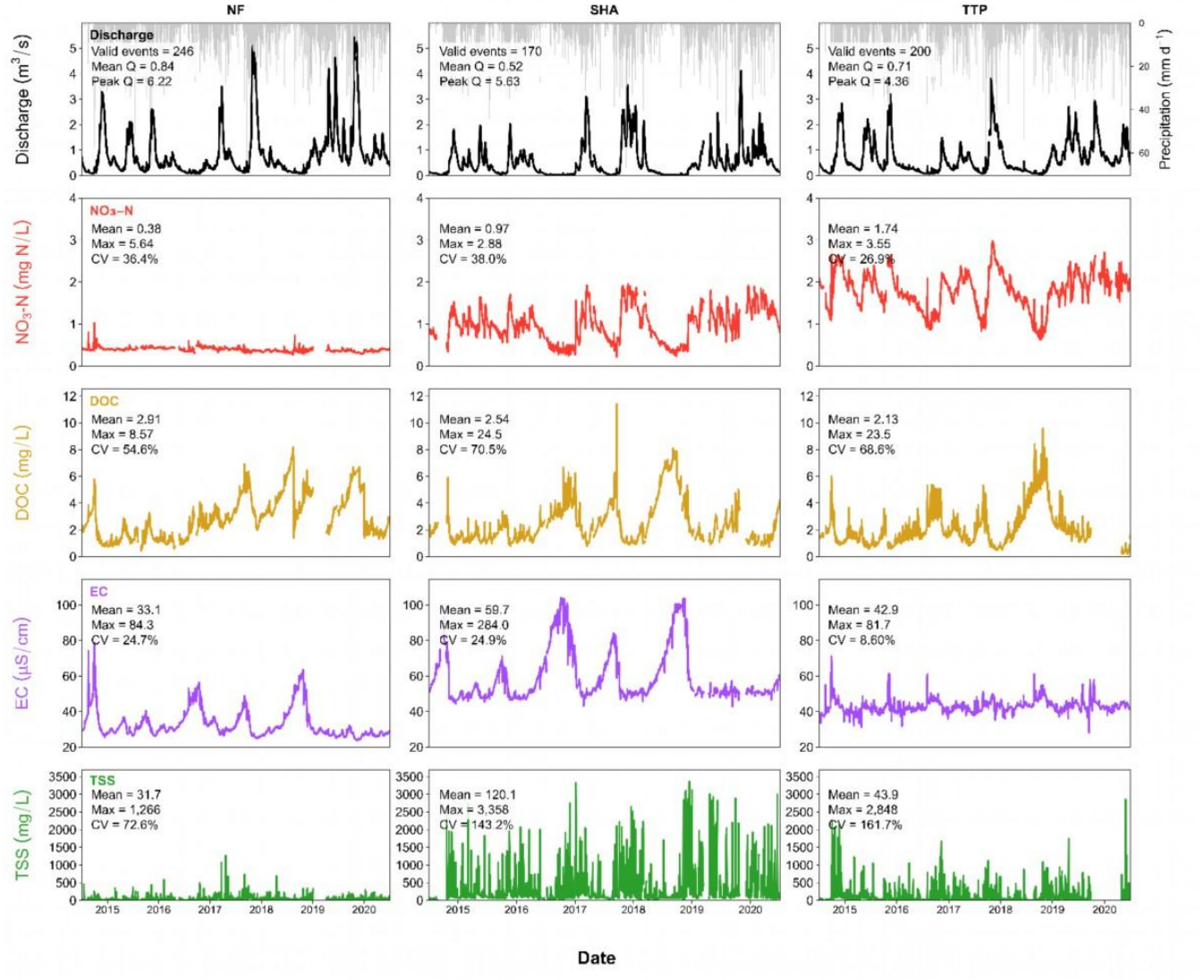


Figure 2. Multi-year (2015–2020) daily hydrochemical time series across three distinct land-use catchments: natural forest (NF), smallholder agriculture (SHA), and tea/tree plantation (TTP). Panels display daily mean discharge paired with inverted daily precipitation totals, daily median nitrate-nitrogen (NO_3–N), dissolved organic carbon (DOC), and electrical conductivity (EC), and daily maximum total suspended solids (TSS). Variable-specific summaries (mean, median, or maximum) are deliberately applied to capture typical dissolved-constituent baselines while simultaneously preserving episodic sediment pulses. Full-record statistics (mean, maximum, and coefficient of variation) derived from the original, non-interpolated 10-minute observations. Gaps denote periods with missing or excluded data.

Table 1. Catchment-scale summary statistics of rainfall, discharge, and hydrochemical variables during the 2015–2020 monitoring period.

	Natural forest				Smallholder agriculture				Tea and tree plantations			
Variable	**Min**	**Mean ± SD**	**Max**	**CV (%)**	**Min**	**Mean ± SD**	**Max**	**CV (%)**	**Min**	**Mean ± SD**	**Max**	**CV (%)**

https://doi.org/10.5194/egusphere-2026-6000
Preprint. Discussion started: 11 November 2026
© Author(s) 2026. CC BY 4.0 License.

	Natural forest				Smallholder agriculture				Tea and tree plantations			
Precipitation (mm 10 min^{-1})	0	0.04 ± 0.29	21.9	788.8	0	0.03 ± 0.22	12.2	745.6	0	0.04 ± 0.28	20.1	789.4
Discharge (m^3 s^{-1})	0.07	0.84 ± 0.96	6.22	114.7	0.01	0.52 ± 0.64	5.63	122.3	0.05	0.71 ± 0.67	4.36	94.9
NO_3–N (mg N L^{-1})	0	0.38 ± 0.14	5.64	36.4	0	0.97 ± 0.37	2.88	38.0	0.08	1.74 ± 0.47	3.55	26.9
DOC (mg L^{-1})	0.4	2.91 ± 1.59	8.57	54.6	0	2.54 ± 1.79	24.5	70.5	0.01	2.13 ± 1.46	23.5	68.6
EC (µS cm^{-1})	14.8	33.1 ± 8.16	84.3	24.7	6.28	59.7 ± 14.9	284.0	24.9	23.8	42.9 ± 3.71	81.7	8.6
TSS (mg L^{-1})	0.0	31.7 ± 23.0	1,266	72.6	0.9	120.1±171.9	3,358	143.2	2.1	43.9 ± 71.0	2,848	161.7

Note. Means are reported as mean ± standard deviation (SD). CV, coefficient of variation; NO_3–N, nitrate; DOC, dissolved organic carbon; EC, electrical conductivity; TSS, total suspended solids

Higher NO_3–N in managed catchments is consistent with greater nutrient availability and nitrate export under agricultural land use (Jacobs et al., 2018b), while surface and subsurface flow regulate when these sources connected to the stream (Jacobs et al., 2018a; Husic et al., 2023; Yue et al., 2023). Similar mean DOC concentrations concealed short-lived carbon pulses associated with transient connection of organic-rich soil and riparian source zones (Vaughan et al., 2017; Bujak-Ozga et al., 2025). Higher TSS in SHA and TTP indicates greater sediment availability and transport connectivity under disturbed land use (Stenfert Kroese et al., 2020), with event magnitude further influenced by rainfall forcing and source availability (Long et al., 2024; Jing et al., 2025; Kim et al., 2026). Higher dry-season EC likely reflects reduced dilution and a greater relative contribution of mineralized groundwater and weathering-derived constituents at low flow (Jacobs et al., 2018a; Zhi et al., 2019). Overall, land use most clearly differentiated NO_3–N and TSS conditions, whereas mean DOC and relative EC variability showed weaker contrasts.

The event-selection criteria identified 695 hydrologically distinct rainfall–runoff responses that could be separated from adjacent events; 279 in NF, 190 in SHA, and 226 in TTP (Fig. 2). These are not all rainfall events in the record. The daily occurrence of rainfall events in the wet season often did not allow discharge and concentrations to return to their initial state, resulting in the exclusion of these rainfall events. Each event was evaluated separately for NO_3–N, DOC, EC, and TSS, with the 90% data-density rule applied by constituent. For the initial-flow analysis, 246 NF, 170 SHA, and 200 TTP events had at least one responsive constituent, a valid HI_{Lloyd} estimate, and an available event-onset discharge (Q_o). These reduced sample sizes reflect the additional response and data-availability requirements rather than a second event-delineation procedure. Q_o was assigned to low-, mid-, or high-flow classes defined from the 33rd and 66th percentiles of the complete six-year daily discharge record. NF comprised 39% low-flow, 36% mid-flow, and 25% high-flow events. This distribution was slightly different for SHA with 28%, 35% and 37% and TTP with 47%, 31% and 23% (Fig. S2). These proportions therefore describe the filtered analytical subset and should not be interpreted as frequencies of all naturally occurring events. The corresponding HI_{Lloyd} distributions showed substantial overlap among initial-flow classes, with catchment- and constituent-specific shifts rather than uniformly separated flow-regime responses (Fig. S1).

https://doi.org/10.5194/egusphere-2026-6000
Preprint. Discussion started: 11 November 2026
© Author(s) 2026. CC BY 4.0 License.

3.2 Storm-event hysteresis and constituent dynamics

Each of the 695 identified rainfall–runoff events were evaluated separately for NO_3–N, DOC, EC, and TSS, allowing one event to contribute up to four event–constituent combinations. Among 2,506 classifiable combinations, chemostasis dominated (70%), followed by mobilization (27%) and dilution (3%) (Table S1). EC (98%), NO_3–N (89%), and DOC (66%) were predominantly chemostatic, whereas TSS was predominantly mobilized (69%). This contrast persisted across catchments: EC and NO_3–N were chemostasis-dominated at all sites; DOC was chemostatic in NF (75%) and SHA (80%) but mobilized in TTP (54%); and TSS was mobilized in NF (62%), SHA (72%), and TTP (76%).

Response frequency, defined as at least one excursion beyond ±15% of C_0 during an event, ranged from 10–23% for EC and 40–54% for NO_3–N to 66–96% for DOC and 98–100% for TSS. Of 1,472 responsive combinations, 1,323 met the geometry criteria and yielded finite HI_{Lloyd} and A_{loop} values with valid loop classifications; the remaining 10% were excluded because valid rising- and falling-limb geometry could not be resolved (Liu et al., 2021; Mazilamani et al., 2024). Mobilization and dilution together represented 51% of responsive combinations, compared with 30% of the full classifiable population. Brief threshold excursions can therefore coexist with an event-level chemostatic classification (Knapp et al., 2020), so response prevalence and dominant chemical status capture complementary aspects of event behaviour (Godsey et al., 2009).

The geometry-resolved analysis provided information about response timing through loop direction (HI_{Lloyd}) and rising–falling-limb separation (A_{loop}), with the assigned loop structures capturing complementary aspects of storm-event transport (Fig. 3). In Fig. 3a-b, positive HI_{Lloyd} indicates concentrations that are generally higher on the rising limb than on the falling limb at equivalent discharge, thus corresponding to clockwise hysteresis loops, negative HI_{Lloyd} indicates higher concentrations on the falling limb and, thus, anticlockwise loops (Lloyd et al., 2016b). A_{loop} measures the magnitude of the separation, and thus difference in timing of the concentration and discharge peaks, regardless of direction (Zuecco et al., 2016). Figure-8/mixed trajectories were the most frequent loop form, representing 61% of the 1,323 geometry-resolved combinations and dominating TSS (70%) and NO_3–N (66%), DOC (50%) and EC (47%) at the pooled constituent level (Fig. 3c). Anticlockwise loops accounted for 49% of DOC and 32% of EC responses, whereas clockwise loops were generally less frequent, and reached their highest pooled contribution for EC (22%).

https://doi.org/10.5194/egusphere-2026-6000
Preprint. Discussion started: 11 November 2026
© Author(s) 2026. CC BY 4.0 License.

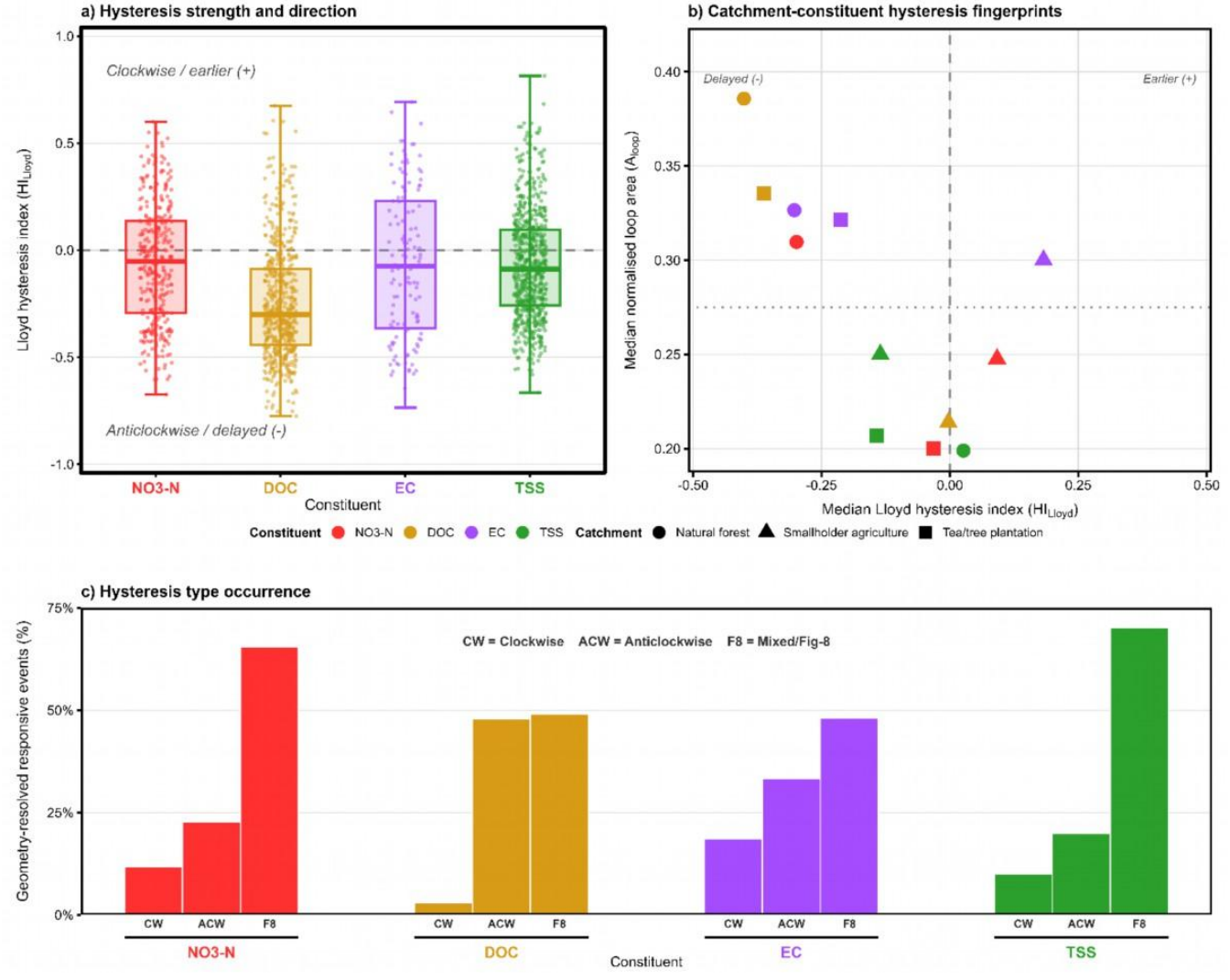


Figure 3. Hysteresis characteristics across constituents and catchments. (a) Distribution of the Lloyd hysteresis index (HI_{Lloyd}) by constituent, with positive values indicating earlier/clockwise delivery and negative values indicating delayed/anticlockwise delivery. (b) Catchment–constituent hysteresis fingerprints based on median HI_{Lloyd} and median normalized loop area (A_{loop}); colours represent constituents and symbols represent catchments. (c) Relative occurrence of clockwise (CW), anticlockwise (ACW), and mixed/Figure-8 (F8) hysteresis types among geometry-resolved responsive event–constituent combinations.

In NF, median HI_{Lloyd} was negative for DOC, EC, and NO_3–N, which, in combination with the positive FI for all constituents, represents anticlockwise hysteresis loop typical for delayed release and transport of constituents. TSS also had a positive FI, but the median HI_{Lloyd} was balanced, with both positive and negative HI_{Lloyd} values (Fig. 3b and 4; Table S2).

https://doi.org/10.5194/egusphere-2026-6000
Preprint. Discussion started: 11 November 2026
© Author(s) 2026. CC BY 4.0 License.

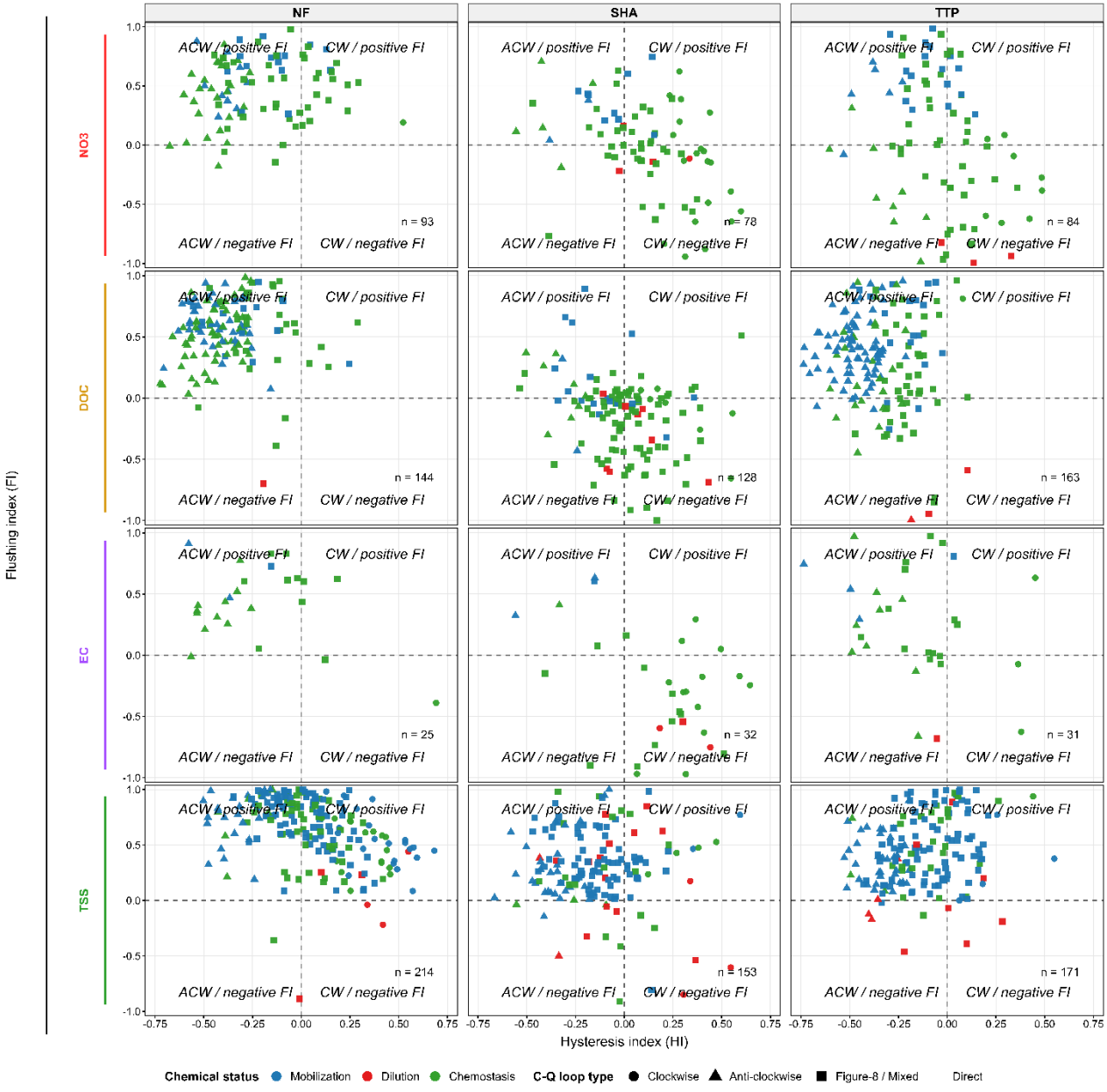


Figure 4. Joint distributions of the Lloyd hysteresis index (HI_{Lloyd}) and flushing index (FI) for responsive event–constituent combinations across NF, SHA, and TTP. Rows show NO_3–N, DOC, EC, and TSS. Colours indicate time-integrated chemical status and symbols indicate C–Q loop type. Dashed reference lines separate falling-limb versus rising-limb dominance ($HI_{Lloyd} = 0$) and depletion versus enrichment at peak discharge relative to event onset (FI = 0). Vaughan FI is bounded from −1 to +1. Coloured row labels indicate constituent identity; point colours indicate chemical status.

https://doi.org/10.5194/egusphere-2026-6000
Preprint. Discussion started: 11 November 2026
© Author(s) 2026. CC BY 4.0 License.

TSS also had a positive FI, but HI_{Lloyd} values were more balanced between positive and negative responses. SHA showed the strongest divergence: EC and NO_3–N tended towards positive HI_{Lloyd}. EC in SHA was also the catchment-constituent combination with the highest occurrence of clockwise hysteresis loops. DOC in SHA was balanced with both positive and negative HI_{Lloyd} values, in contrast to NF and TTP, where anticlockwise loops were predominant. This suggests a shift in DOC mobilisation and transport and could be related to the presence of dense vegetation along the streams in NF and TTP, delivering organic matter to the soil that is mobilised during rainfall events. A_{loop} was largest for DOC in NF and TTP, indicative of the mobilisation of more distant sources. In contrast, dilution of DOC in SHA, as indicated by the generally negative FI (Fig. 4), suggests source limitation and a large contribution of event water with low DOC concentrations. TSS concentrations were higher on the falling limb, suggesting activation of distant sediment sources in SHA, although the values for A_{loop} were not very high. Several other managed-catchment dissolved-constituent responses also showed smaller A_{loop} values, potentially due to more rapid constituent responses in managed catchments due to activation of surface flowpaths. In TTP, DOC, EC, and TSS were dominated by negative HI_{Lloyd} values and positive FI, whereas NO_3–N was balanced both in terms of HI_{Lloyd} and of FI. Representative storm hydrographs further illustrate how rainfall sequencing, discharge response, and constituent concentration timing differed among NF, SHA, and TTP (Fig. 5). The corresponding normalized C–Q trajectories show how these temporal responses translated into figure-8/mixed, anticlockwise, and clockwise hysteresis geometries, including rising–falling-limb separation, crossings, and directional reversals (Fig. 6).

https://doi.org/10.5194/egusphere-2026-6000
Preprint. Discussion started: 11 November 2026
© Author(s) 2026. CC BY 4.0 License.

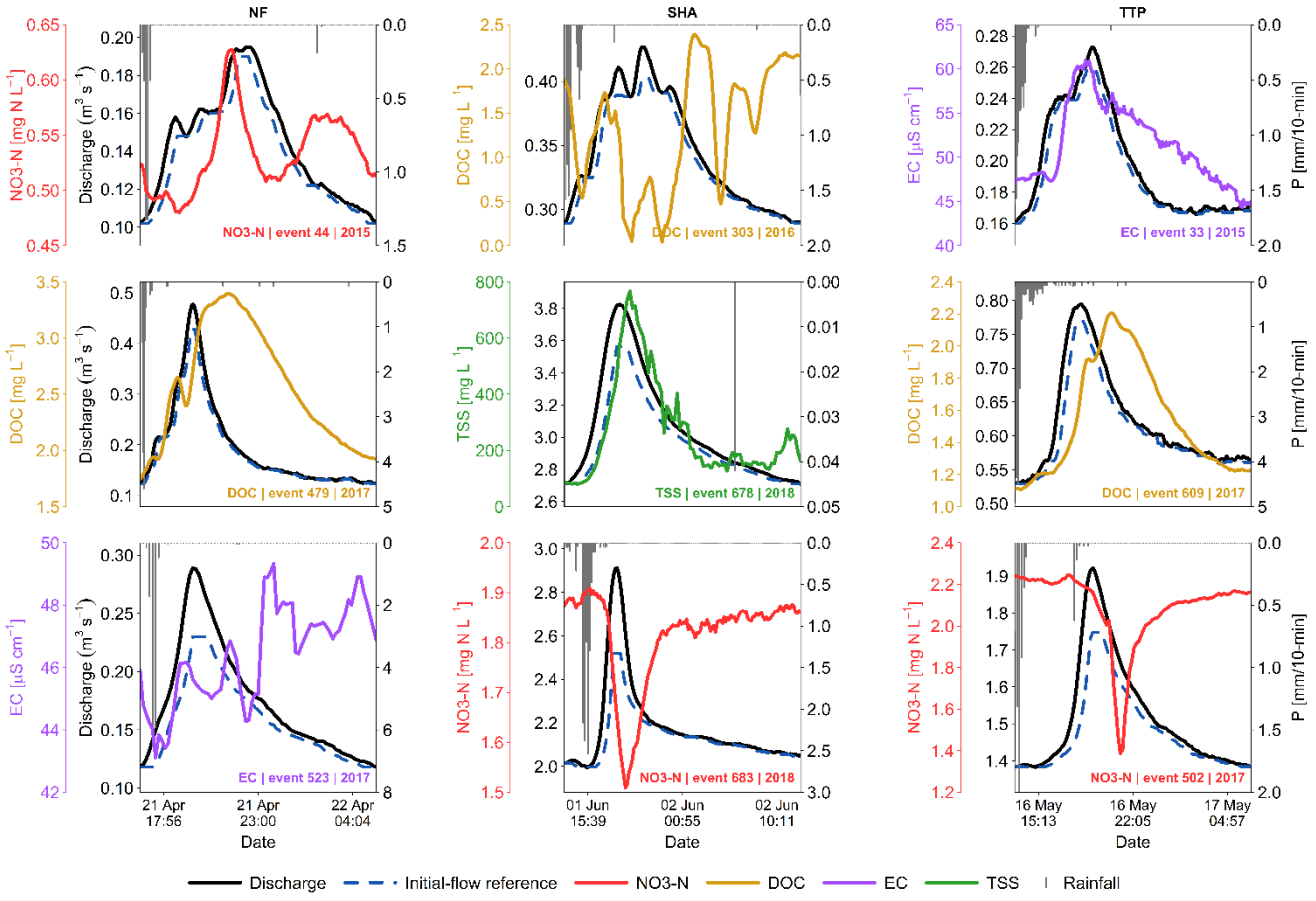
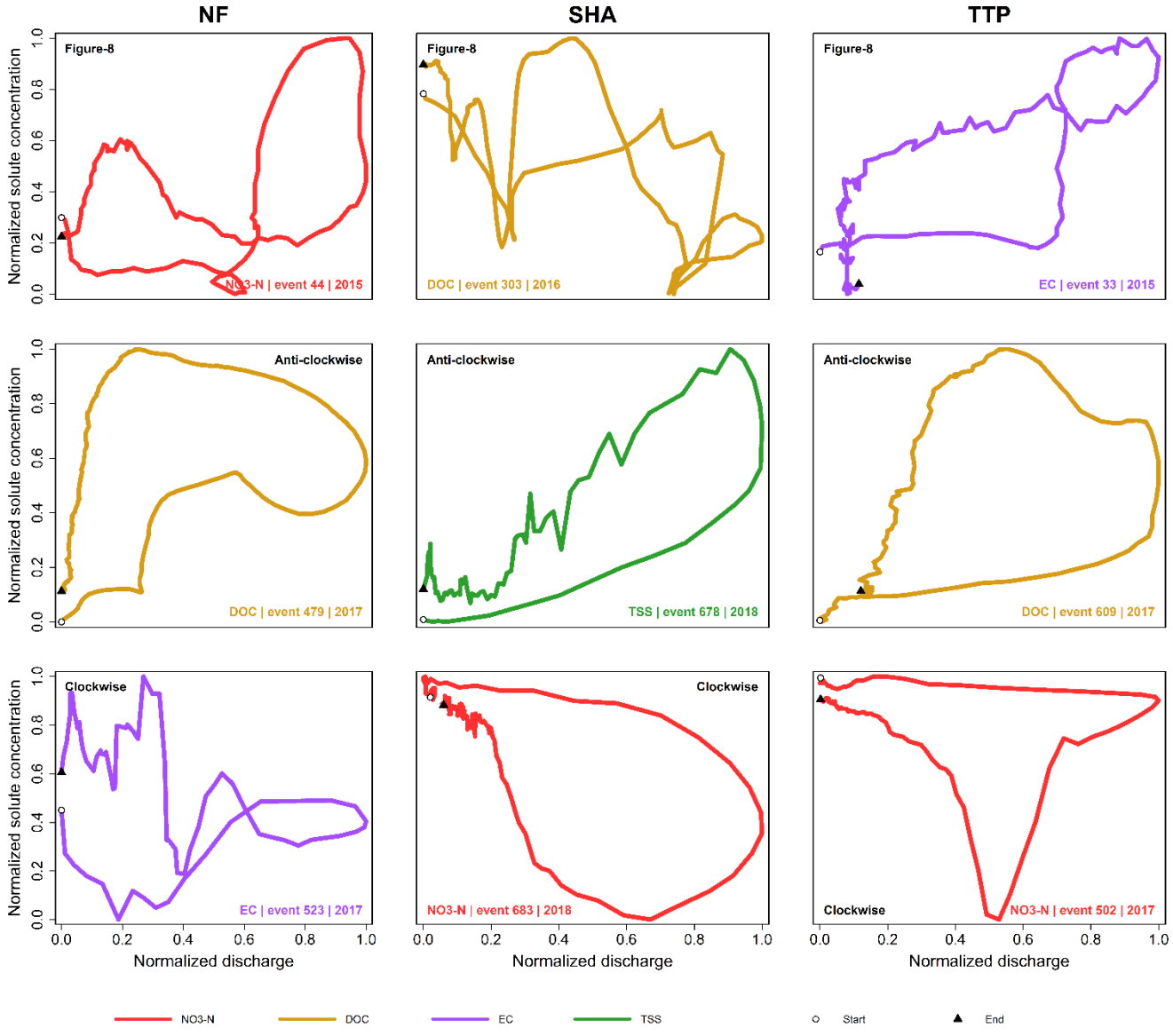


Figure 5. Representative storm hydrographs and constituent responses across the South-West Mau catchments. Columns show natural forest (NF), smallholder agriculture (SHA), and tea/tree plantation (TTP). Panels display rainfall, measured discharge, the baseflow or initial-flow reference, and constituent concentration, illustrating whether concentration maxima occurred before, near, or after peak discharge.

https://doi.org/10.5194/egusphere-2026-6000
Preprint. Discussion started: 11 November 2026
© Author(s) 2026. CC BY 4.0 License.



355 **Figure 6.** Hysteresis loops defined by normalized concentration–discharge trajectories for the events shown in Fig.5. Columns show NF, SHA, and TTP, while rows show figure-8/mixed, anticlockwise, and clockwise examples. Colour indicates event progression from start to end. The trajectories show rising–falling-limb separation, crossings, directional reversals, delayed delivery, and early enrichment.

3.3 Integrated multivariate storm-event response patterns

360 Joint analysis of HI_{Lloyd}, A_{loop}, and FI identified three stable, recurrent transport patterns whose probability of occurrence shifted dynamically with hydrograph structure and weather forcing across the landscape gradient (Table 2; Fig. S3-S5).

https://doi.org/10.5194/egusphere-2026-6000
Preprint. Discussion started: 11 November 2026
© Author(s) 2026. CC BY 4.0 License.

Evaluating these clusters alongside their underlying hydrological distributions and cluster stability diagnostics (Fig. S3–S5) demonstrates that catchments do not exhibit a single fixed response but rather shift between distinct behavioural zones.

3.3.1 Response-cluster structure and catchment–constituent patterns

The 1,323 geometry-resolved event–constituent combinations formed three reproducible regions within a continuous response space (Fig. S5; Table 2). The partitioning-around-medoids solution at k=3 had the highest average silhouette width (0.350), indicating meaningful but incomplete separation among clusters (Fig. S5a; Kaufman and Rousseeuw, 1990). Resampling confirmed high stability, with mean bootstrap–Jaccard similarities of 0.946, 0.913, and 0.884 for the three clusters (Fig. S5c). Silhouette distributions nevertheless overlapped and included some values near or below zero (Fig. S5b), supporting interpretation as stable response regions rather than discrete mechanistic classes (Hennig, 2007). Cluster membership differed strongly among catchment–constituent combinations ($\chi^2_{22} = 703.1$, $q < 0.001$; Fig. S4c; Table 2), consistent with evidence that land use and constituent type jointly structure storm-event hysteresis, hydrological pathways, and constituent export (Vaughan et al., 2017; Jacobs et al., 2018a, 2018b; Husic et al., 2023).

The three clusters differed systematically in prevalence, loop direction, response timing, and flushing behaviour (Table 2). C1 contained 437 combinations (33%) and combined anticlockwise loop dominance (median $HI_{Lloyd} = -0.410$), the greatest separation between rising and falling limb concentrations (median $A_{loop} = 0.395$), and positive FI (median = 0.419); 75% of its loops were anticlockwise. These characteristics point to events mobilising more distant sources, such as riparian, hillslope or subsurface storage of solutes and could be characterised as “delayed flushing” responses. This cluster was dominated by DOC (52%), particularly in NF and TTP, potentially due to the flushing of dissolved organic matter from the intact riparian zones. NO_3–N and EC responses in NF also occurred frequently in this cluster.

C2 contained 443 combinations (34%) and was balanced overall (median $HI_{Lloyd} = +0.036$), with moderate separation ($A_{loop} = 0.204$), weak slightly negative net FI (−0.027), and predominantly figure-8/mixed loops (76%). These characteristics suggest complex response patterns with loop direction reversal, potentially related to the mobilisation of different solute sources within the catchment (Butturini et al., 2008; Roberts et al., 2023), and could be characterised as “rapid mixed response”. DOC, NO_3–N and EC responses in SHA and NO_3–N in TTP dominated this cluster. As groundwater is considered the major source of NO_3–N in both SHA and TTP (Jacobs et al. 2018), there would be little mobilisation during rainfall events and higher chances of dilution, as event water likely has lower solute concentrations.

C3 contained 439 combinations (33%) and combined low HI_{Lloyd} values (median of −0.064), low separation ($A_{loop} = 0.186$), and the strongest positive FI (0.691); figure-8/mixed loops accounted for 81%. The cluster, typical for “rapid flushing” responses of suspended sediments (Roberts et al., 2023; Jing et al., 2025; Long et al., 2024), was dominated by TSS responses (66%) with the strongest occurrence in NF followed by TTP, suggesting that sediments originate close to the stream. In TTP, the drainage network could also lead to rapid discharge of surface runoff rich in sediments into the stream. While paths and tracks in SHA also function as sediment conduits between crop fields and the streams (Stenfert Kroese et al. 2020), larger sources and longer flow paths could lead to a slower response to rainfall.

https://doi.org/10.5194/egusphere-2026-6000
Preprint. Discussion started: 11 November 2026
© Author(s) 2026. CC BY 4.0 License.

Table 2. Integrated response-cluster profiles, catchment–constituent enrichment, and hydrological context.

Cluster C1	Cluster C2	Cluster C3
Panel A. Multivariate response profiles (n = 1,319; PAM k = 3; mean silhouette = 0.350)		
Delayed Flushing	**Rapid Mixed Response**	**Rapid Flushing**
n = 437 combinations (33%) Mean Jaccard = 0.946 Median HI_{Lloyd} = -0.410 Median A_{loop} = 0.395 Median FI = 0.419 Figure-8/mixed: 25% Anticlockwise: 75% Clockwise: 0% Profile: falling-limb dominant; high-separation; positive-FI flushing	n = 443 combinations (34%) Mean Jaccard = 0.913 Median HI_{Lloyd} = +0.036 Median A_{loop} = 0.204 Median FI= -0.027 Figure-8/mixed: 76% Anticlockwise: 6% Clockwise: 18% Profile: balanced-limb; moderate-separation; weak-net-FI flushing	n = 439 combinations (33%) Mean Jaccard = 0.884 Median HI_{Lloyd} = -0.064 Median A_{loop} = 0.186 Median FI= 0.691 Figure-8/mixed: 81% Anticlockwise: 12% Clockwise: 7% Profile: falling-limb dominant; low-separation; positive-FI flushing
Panel B. Catchment-constituent enrichment (χ^2_{22} = 703.1; q < 0.001)		
Delayed dissolved-constituent enrichment	**Managed-catchment dissolved-constituent enrichment**	**Sediment-dominated enrichment**
Dominant constituent: DOC = 229/437 (52%) NF DOC: n = 107; residual = +10.93; O/E = 2.21 TTP DOC: n = 110; residual = +9.87; O/E = 2.02 NF NO3-N: n = 50; residual = +4.38; O/E = 1.62 NF EC: n = 13; residual = +2.02; O/E = 1.57	Dominant constituent: DOC = 150/443 (34%) SHA DOC: n = 114; residual = +13.99; O/E = 2.65 SHA NO3-N: n = 61; residual = +8.60; O/E = 2.33 SHA EC: n = 27; residual = +6.16; O/E = 2.51 TTP NO3-N: n = 45; residual = +4.01; O/E = 1.60	Dominant constituent: TSS = 291/439 (66%) NF TSS: n = 151; residual = +12.64; O/E = 2.12 TTP TSS: n = 88; residual = +5.41; O/E = 1.55 NF EC: n = 9; residual = +0.29; O/E = 1.08 TTP NO3-N: n = 29; residual = +0.25; O/E = 1.04

https://doi.org/10.5194/egusphere-2026-6000
Preprint. Discussion started: 11 November 2026
© Author(s) 2026. CC BY 4.0 License.

Panel C. Hydrograph structure and hydrological context		
Delayed / drier-state tendency	**Recurrent-wave / mixed-response tendency**	**Rapid-flushing / higher-rainfall tendency**
Multiple rain pulses: 71%	Multiple rain pulses: 68%	Multiple rain pulses: 71%
Multiple discharge peaks: 14%	Multiple discharge peaks: 27%	Multiple discharge peaks: 19%
Either compound feature: 76%	Either compound feature: 76%	Either compound feature: 77%
Mean Qpeak count: 1.08	Mean Qpeak count: 1.26	Mean Qpeak count: 1.14
Median peak separation: 5.3 h	Median peak separation: 5.6 h	Median peak separation: 5.5 h
Rain: 9.2 mm (IQR 5.91-14.70)	Rain: 8.9 mm (IQR 5.40-14.08)	Rain: 10.5 mm (IQR 6.77-16.01)
Imax: 16.1 mm/h (IQR 9.76-26.87)	Imax: 15.9 mm/h (IQR 9.52-24.09)	Imax: 17.0 mm/h (IQR 10.90-27.20)
Dry period: 22.8 h (IQR 17.67-48.50)	Dry period: 20.7 h (IQR 16.50-37.33)	Dry period: 21.7 h (IQR 17.42-46.58)
Pre-event TSS: 41.9 mg/L (IQR 23.86-65.45)	Pre-event TSS: 41.4 mg/L (IQR 22.09-60.96)	Pre-event TSS: 32.3 mg/L (IQR 20.55-44.15)

Note. Cluster labels describe recurrent response regions rather than completely discrete mechanistic classes. Positive enrichment residuals identify catchment–constituent combinations occurring more frequently than expected. Catchment, constituent, and joint catchment–constituent associations were all significant ($q < 0.001$). Multiple discharge peaks differed among clusters ($\chi^2_2 = 15.29$, $q = 0.00067$), whereas multiple rainfall pulses ($\chi^2_2 = 1.55$, $q = 0.538$) and the broad compound-hydrograph category ($\chi^2_2 = 0.83$, $q = 0.659$) did not. Event rainfall, maximum rainfall intensity, and discharge-peak count differed at $q = 0.002$, and antecedent dry period at $q = 0.007$. Hydrological values are descriptive medians and interquartile ranges (IQRs); their extensive overlap indicates associated context rather than deterministic control. PAM, partitioning around medoids; HI_{Lloyd}, Lloyd hysteresis index; A_{loop}, normalized loop area; FIpeak, peak flushing intensity; Imax, maximum rainfall intensity; Qpeak, discharge-peak count; q, false-discovery-rate-adjusted p-value. O/E, observed-to-expected ratio; values >1 indicate overrepresentation and values <1 indicate underrepresentation of a catchment–constituent combination within a cluster.

https://doi.org/10.5194/egusphere-2026-6000
Preprint. Discussion started: 11 November 2026
© Author(s) 2026. CC BY 4.0 License.

3.3.2 Hydrograph structure and adjusted environmental associations

Multiple discharge peaks occurred in 14% of C1, 27% of C2, and 19% of C3 combinations and showed a clearer group contrast. Recurrent discharge waves were therefore most frequent in C2 but were not exclusive to any response region. Such waves can generate overlapping concentration responses, crossings, and cancellation within HI_{Lloyd} (Butturini et al., 2008; Vaughan et al., 2017; Mazilamani et al., 2024), thus explaining the frequent occurrence of figure-8 hysteresis loops in this cluster. Antecedent dry period and discharge-peak count differed among response groups after false-discovery-rate correction (both BH $q < 0.001$), and event rainfall also differed ($q = 0.013$), whereas maximum rainfall intensity did not ($q = 0.263$; Fig. S6). Median event rainfall was highest in C3 (10.5 mm) compared with C1 (9.2 mm) and C2 (8.9 mm), while median antecedent dry periods were similar, but the distributions differed, with a long upper tail in all groups. Maximum rainfall intensity showed extensive overlap and should therefore not be interpreted as an overall differentiating factor. The broad overlap across all four hydrological distributions reinforces that these variables describe probabilistic context rather than exclusive response domains. Antecedent conditions can influence source availability and hydrological connectivity (Bujak-Ozga et al., 2025; Huang et al., 2025; Yue et al., 2023), while event rainfall can modulate mobilization opportunities without uniquely determining response-group membership.

After adjustment for catchment–constituent composition, the largest response-group probability range for antecedent dry period occurred for C2, whose adjusted probability declined from about 36% at the short-dry-period end of the observed range to about 18% at the longest dry periods (Fig. 7a). C2 probability was approximately 33% for zero qualifying internal discharge peaks, 32% for one peak, 40% for two peaks, and 61% for three or more peaks (Fig. 7b), consistent with a stronger association with recurrent discharge waves after adjustment. For event rainfall, C1 showed the largest adjusted range, declining from about 40% under the lowest rainfall to about 27% at the upper observed range (Fig. 7c). C1 also showed the largest modelled range for maximum rainfall intensity, with a shallow U-shaped pattern; however, maximum intensity did not differ significantly among response groups in the overall Kruskal–Walli's analysis (BH $q = 0.263$), so this panel is interpreted descriptively rather than as evidence of a general group difference (Fig. 7d). The broad confidence and transition bands indicate gradual, sample-dependent associations rather than deterministic thresholds. Previous studies have shown that storm-event characteristics, including antecedent wetness, rainfall magnitude, discharge response, and source availability, can strongly influence event-scale C–Q and hysteresis behaviour (Knapp et al., 2020; Musolff et al., 2021; Husic et al., 2023; Huang et al., 2025). Our results are consistent with these event-scale controls but indicate that their effects were superimposed on a stronger catchment–constituent structure. In particular, cluster membership was more clearly organized by land-use setting and constituent identity, while antecedent dry period, discharge-peak recurrence, and event rainfall modified the probability of individual response patterns. This suggests that storm forcing determines when particular responses are expressed, whereas source availability and hydrological pathways associated with land use and constituent type provide the broader template within which those responses occur. Overall, catchment–constituent setting remained the stronger organizing factor, while hydrological conditions slightly modified response-group probabilities.

https://doi.org/10.5194/egusphere-2026-6000
Preprint. Discussion started: 11 November 2026
© Author(s) 2026. CC BY 4.0 License.

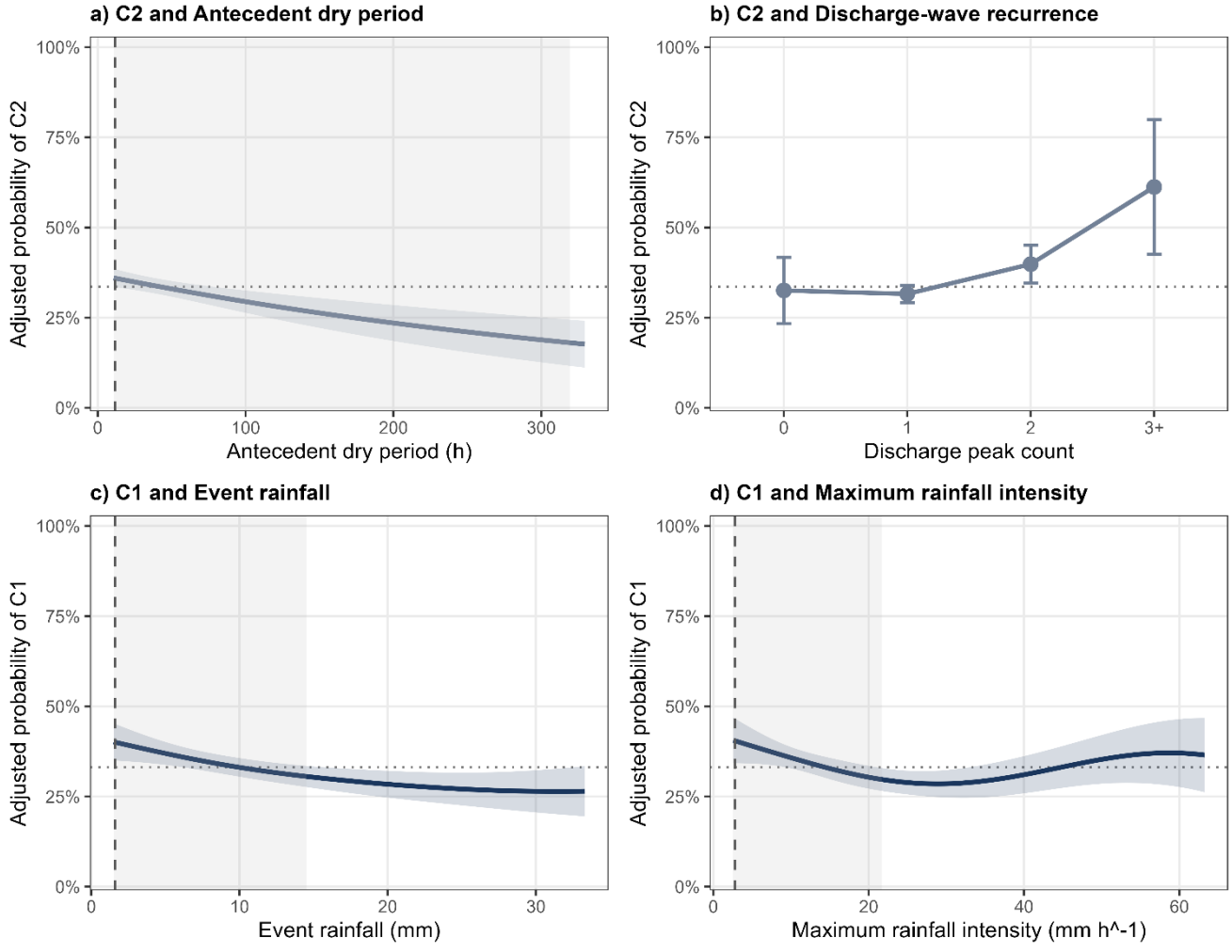


Figure 7. Adjusted probabilities of multivariate response-group membership in relation to selected hydrological signatures after accounting for catchment–constituent composition. Panels show the probability of C2 membership across (a) antecedent dry period and (b) discharge-peak-count categories, and the probability of C1 membership across (c) event rainfall and (d) maximum rainfall intensity. Solid curves or points represent adjusted probabilities, with pointwise 95% confidence intervals shown by shaded ribbons or error bars. Horizontal dotted lines indicate the overall prevalence of the corresponding response group. For the continuous predictors, dashed vertical lines identify the point of greatest absolute probability change, and shaded vertical bands indicate the associated transition range; these features represent sample-dependent changes in probability rather than deterministic thresholds.

4. Conclusions

Hysteresis metrics revealed distinct land-use-dependent stormflow response signatures across the South-West Mau catchments. NF was characterized predominantly by delayed responses of DOC, EC, and NO_3–N to rainfall events, whereas managed catchments showed more rapid event responses. SHA differed most clearly for NO_3–N and EC, which more often showed positive HILloyd and clockwise behaviour, whereas DOC in SHA frequently showed dilution during responsive

https://doi.org/10.5194/egusphere-2026-6000
Preprint. Discussion started: 11 November 2026
© Author(s) 2026. CC BY 4.0 License.

events. TTP retained delayed DOC and EC responses together with strong TSS mobilization. TSS was predominantly mobilized in all catchments, with substantially higher absolute concentrations in SHA and TTP than in NF. Land use therefore affected both constituent response magnitude and within-event timing, but not through a uniform forest-to-managed shift. These differences were expressed through loop direction, response timing and flushing behaviour as represented by HI_{Lloyd}, A_{loop} and FI. The membership of events to one of the three resulting clusters were not determined by individual storm characteristics alone. Rather, each cluster represented a specific land-use constituent combination. The "delayed flushing" cluster included solutes characterised by mobilisation (DOC in TTP and NF, as well as EC and NO3-N in NF), the "rapid mixed response" cluster was dominated by solutes in managed catchments, showing complex hysteresis patterns typical of sequential source activation, and the "rapid flushing" cluster represented TSS mobilisation in all catchments, whereby NF showed the fastest response to rainfall events. Overall, high-frequency monitoring combined with hysteresis metrics revealed land-use-dependent transport dynamics that are obscured by event-mean concentrations or low-frequency sampling. These observed patterns point to differences in hydrological connectivity and source activation among land use types, which can inform interventions to reduce nutrient and soil losses and strengthen the ability of landscapes to regulate water quality.

Code and data availability

The 10-minute resolution hydro-meteorological and hydrochemical dataset used in this study for the period 2015–2020 is publicly archived in Zenodo (Tabo et al., 2026) at https://doi.org/10.5281/zenodo.23078064. The R code used for rainfall–runoff event detection, calculation of event and hysteresis metrics, chemical-status classification, multivariate response clustering, statistical analyses, and reproduction of the manuscript figures and tables is available in the GitHub repository https://github.com/jluzt2022/mau-hysteresis-reproducibility, release v1.0.0.

Supplement

The supplement related to this article contains additional tables and figures supporting the analyses presented in the main text.

Author contributions

ZT: writing – original draft, software, methodology, formal analysis, and visualization. LB: conceptualization, supervision, investigation, funding acquisition, project administration, and writing – review and editing. SRJ: methodology, data curation, investigation, supervision, project administration, and writing – review and editing.

Competing interests

The authors declare that they have no conflict of interest.

https://doi.org/10.5194/egusphere-2026-6000
Preprint. Discussion started: 11 November 2026
© Author(s) 2026. CC BY 4.0 License.

Acknowledgements

We gratefully acknowledge the Kenya Forest Service (KFS) for granting access to and facilitating research activities in the Mau Forest. We also thank CIFOR for administrative support, as well as the PhD students, field assistants, security personnel, and drivers whose sustained efforts contributed to the operation and maintenance of the hydro-meteorological monitoring network throughout the study period.

Financial support

This study was funded by the German Research Foundation (Deutsche Forschungsgemeinschaft, DFG) through the project "Global change impact on hydro-biogeochemical processes in tropical Kenyan catchments" (project number 280246701, grant BR2238/23-2).

References

Benjamini, Y. and Hochberg, Y.: Controlling the false discovery rate: A practical and powerful approach to multiple testing, J. Roy. Stat. Soc. B, 57, 289–300, https://doi.org/10.1111/j.2517-6161.1995.tb02031.x , 1995.

Binge, F. W.: Geology of the Kericho Area, Report No. 50, Geological Survey of Kenya, 1962.

Bracken, L. J., Wainwright, J., Ali, G. A., Tetzlaff, D., Smith, M. W., Reaney, S., and Roy, A. G.: Concepts of hydrological connectivity: Research approaches, pathways and future agendas, Earth-Sci. Rev., 119, 17–34, https://doi.org/10.1016/j.earscirev.2013.02.001, 2013.

Brandt, P., Hamunyela, E., Herold, M., de Bruin, S., Verbesselt, J., and Rufino, M. C.: Sustainable intensification of dairy production can reduce forest disturbance in Kenyan montane forests, Agr. Ecosyst. Environ., 265, 307–319, https://doi.org/10.1016/j.agee.2018.06.011, 2018.

Bücker, A., Crespo, P., Frede, H.-G., and Breuer, L.: Solute behaviour and export rates in neotropical montane catchments under different land-uses, J. Trop. Ecol., 27, 305–317, https://doi.org/10.1017/S0266467410000787, 2011.

Bujak-Ozga, I., von Freyberg, J., Zimmer, M., Rinaldo, A., Benettin, P., and van Meerveld, I.: Changes in the flowing drainage network and stream chemistry during rainfall events for two pre-Alpine catchments, Hydrol. Earth Syst. Sci., 29, 2339–2359, https://doi.org/10.5194/hess-29-2339-2025, 2025.

Butturini, A., Gallart, F., Latron, J., Vázquez, E., and Sabater, F.: Cross-site comparison of variability of DOC and nitrate c–q hysteresis during the autumn–winter period in three Mediterranean headwater streams: A synthetic approach, Biogeochemistry, 77, 327–349, https://doi.org/10.1007/s10533-005-0711-7, 2006.

Butturini, A., Alvarez, M., Bernal, S., Vázquez, E., and Sabater, F.: Diversity and temporal sequences of forms of DOC and NO_3–discharge responses in an intermittent stream: Predictable or random succession? J. Geophys. Res.-Biogeo., 113, G03016, https://doi.org/10.1029/2008JG000721, 2008.

https://doi.org/10.5194/egusphere-2026-6000
Preprint. Discussion started: 11 November 2026
© Author(s) 2026. CC BY 4.0 License.



Delesantro, J. M., Duncan, J. M., Riveros-Iregui, D., Whitmore, K. M., and Band, L. E.: High frequency monitoring and nitrate sourcing reveals baseflow and stormflow controls on total dissolved nitrogen and carbon export along a rural–urban gradient, Water Resour. Res., 60, e2023WR036750, https://doi.org/10.1029/2023WR036750, 2024.

Edwards, K. A. and Blackie, J. R.: Results of the East African catchment experiments 1958–1974, in: Tropical Agricultural Hydrology, edited by: Lal, R. and Russell, E. W., John Wiley & Sons, 163–188, 1981.

Evans, C. and Davies, T. D.: Causes of concentration/discharge hysteresis and its potential as a tool for analysis of episode hydrochemistry, Water Resour. Res., 34, 129–137, https://doi.org/10.1029/97WR01881, 1998.

Godsey, S. E., Kirchner, J. W., and Clow, D. W.: Concentration–discharge relationships reflect chemostatic characteristics of US catchments, Hydrol. Process., 23, 1844–1864, https://doi.org/10.1002/hyp.7315, 2009.

Hennig, C.: Cluster-wise assessment of cluster stability, Comput. Stat. Data An., 52, 258–271, https://doi.org/10.1016/j.csda.2006.11.025, 2007.

Hong, Y., Adler, R. F., Hossain, F., Curtis, S., and Huffman, G. J.: A first approach to global runoff simulation using satellite rainfall estimation, Water Resour. Res., 43, W08502, https://doi.org/10.1029/2006WR005739, 2007.

Huang, Y., Wang, J., Yao, H., Gu, C., Xu, J., Yin, W., Li, X., Liu, X., Zhu, Z., Jiang, H., Li, H., Yang, L., Xiao, H., and Shi, Z.: High-frequency sampling reveals storm responses to nitrate hysteresis patterns and export characteristics in an agricultural catchment, J. Hydrol., 662, 134091, https://doi.org/10.1016/j.jhydrol.2025.134091, 2025.

Husic, A., Fox, J. F., Clare, E., Mahoney, T., and Zarnaghsh, A.: Nitrate hysteresis as a tool for revealing storm-event dynamics and improving water-quality model performance, Water Resour. Res., 59, e2022WR033180, https://doi.org/10.1029/2022WR033180, 2023.

Jacobs, S. R., Timbe, E., Weeser, B., Rufino, M. C., Butterbach-Bahl, K., and Breuer, L.: Assessment of hydrological pathways in East African montane catchments under different land use, Hydrol. Earth Syst. Sci., 22, 4981–5000, https://doi.org/10.5194/hess-22-4981-2018, 2018a.

Jacobs, S. R., Weeser, B., Guzha, A. C., Rufino, M. C., Butterbach-Bahl, K., Windhorst, D., and Breuer, L.: Using high-resolution data to assess land use impact on nitrate dynamics in East African tropical montane catchments, Water Resour. Res., 54, 1812–1830, https://doi.org/10.1002/2017WR021592, 2018b.

Jing, T., Zeng, Y., Fang, N., Dai, W., and Shi, Z.: A review of suspended sediment hysteresis, Water Resour. Res., 61, e2024WR037216, https://doi.org/10.1029/2024WR037216, 2025.

Kaufman, L. and Rousseeuw, P. J.: Finding Groups in Data: An Introduction to Cluster Analysis, John Wiley & Sons, https://doi.org/10.1002/9780470316801, 1990.

Kim, D., Roberts, M. E., Lu, J., Orr, D. N., and Hamilton, D. P.: Hysteresis during storm events impacts stream sediment and nutrient load calculations, J. Hydrol., 670, 135216, https://doi.org/10.1016/j.jhydrol.2026.135216, 2026.

Knapp, J. L. A., von Freyberg, J., Studer, B., Kiewiet, L., and Kirchner, J. W.: Concentration–discharge relationships vary among hydrological events, reflecting differences in event characteristics, Hydrol. Earth Syst. Sci., 24, 2561–2576, https://doi.org/10.5194/hess-24-2561-2020, 2020.

https://doi.org/10.5194/egusphere-2026-6000
Preprint. Discussion started: 11 November 2026
© Author(s) 2026. CC BY 4.0 License.

Krhoda, G. O.: The impact of resource utilization on the hydrology of the Mau Hills Forest in Kenya, Mt. Res. Dev., 8, 193–200, https://doi.org/10.2307/3673447, 1988.

Leys, C., Ley, C., Klein, O., Bernard, P., and Licata, L.: Detecting outliers: Do not use standard deviation around the mean, use absolute deviation around the median, J. Exp. Soc. Psychol., 49, 764–766, https://doi.org/10.1016/j.jesp.2013.03.013, 2013.

Lintern, A., Webb, J. A., Ryu, D., Liu, S., Bende-Michl, U., Waters, D., Leahy, P., Wilson, P., and Western, A. W.: Key factors influencing differences in stream water quality across space, WIREs Water, 5, e1260, https://doi.org/10.1002/wat2.1260, 2018.

Liu, W., Birgand, F., Tian, S., and Chen, C.: Event-scale hysteresis metrics to reveal processes and mechanisms controlling constituent export from watersheds: A review, Water Res., 200, 117254, https://doi.org/10.1016/j.watres.2021.117254, 2021.

Lloyd, C. E. M., Freer, J. E., Johnes, P. J., and Collins, A. L.: Using hysteresis analysis of high-resolution water-quality monitoring data, including uncertainty, to infer controls on nutrient and sediment transfer in catchments, Sci. Total Environ., 543, 388–404, https://doi.org/10.1016/j.scitotenv.2015.11.028, 2016a.

Lloyd, C. E. M., Freer, J. E., Johnes, P. J., and Collins, A. L.: Technical note: Testing an improved index for analysing storm discharge–concentration hysteresis, Hydrol. Earth Syst. Sci., 20, 625–632, https://doi.org/10.5194/hess-20-625-2016, 2016b.

Long, Y., Lei, M., Li, T., Xiao, P., Liu, S., Xu, J., Tang, F., Hu, X., Hu, X., Nie, X., Li, Z., and Liu, Y.: Suspended sediment–discharge hysteresis characteristics and controlling factors in a small watershed of southern China, Catena, 243, 108198, https://doi.org/10.1016/j.catena.2024.108198, 2024.

Mazilamani, L. S., Walsh, R. P. D., Annammala, K. V., Bidin, K., Yusop, Z., Reynolds, G., and Nainar, A.: Concentration–discharge hysteresis: Current approaches and future directions for quantifying pollutant dynamics in storm events, with a particular focus on the tropics, Sustain. Water Resour. Manag., 10, 156, https://doi.org/10.1007/s40899-024-01130-2, 2024.

Musolff, A., Zhan, Q., Dupas, R., Minaudo, C., Fleckenstein, J. H., Rode, M., Dehaspe, J., and Rinke, K.: Spatial and temporal variability in concentration–discharge relationships at the event scale, Water Resour. Res., 57, e2020WR029442, https://doi.org/10.1029/2020WR029442, 2021.

NASA JPL: NASA Shuttle Radar Topography Mission Global 1 arc second, NASA Land Processes Distributed Active Archive Center [data set], https://doi.org/10.5067/MEASURES/SRTM/SRTMGL1.003, 2013, accessed 1 July 2026.

Roberts, M. E., Kim, D., Lu, J., and Hamilton, D. P.: HARP: A suite of parameters to describe the hysteresis of streamflow and water quality constituents, J. Hydrol., 626, 130262, https://doi.org/10.1016/j.jhydrol.2023.130262, 2023.

Rousseeuw, P. J. and Croux, C.: Alternatives to the median absolute deviation, J. Am. Stat. Assoc., 88, 1273–1283, https://doi.org/10.1080/01621459.1993.10476408, 1993.

Stenfert Kroese, J., Jacobs, S. R., Tych, W., Breuer, L., Quinton, J. N., and Rufino, M. C.: Tropical montane forest conversion is a critical driver for sediment supply in East African catchments, Water Resour. Res., 56, e2020WR027495, https://doi.org/10.1029/2020WR027495, 2020.

Swart, R.: Monitoring 40 years of land use change in the Mau Forest Complex, Kenya: A land use change driver analysis, MSc thesis, Wageningen University, Wageningen, the Netherlands, 2016.

https://doi.org/10.5194/egusphere-2026-6000
Preprint. Discussion started: 11 November 2026
© Author(s) 2026. CC BY 4.0 License.

Tabo, Z., Jacobs, S. R., and Breuer, L.: 10-minute hydro-meteorological and hydrochemical data for storm-event hysteresis analysis in South-West Mau, Kenya (2015–2020), Zenodo [data set], https://doi.org/10.5281/zenodo.23078064, 2026.

Vaughan, M. C. H., Bowden, W. B., Shanley, J. B., Vermilyea, A., Sleeper, R., Gold, A. J., Pradhanang, S. M., Inamdar, S. P., Levia, D. F., Andres, A. S., Birgand, F., and Schroth, A. W.: High-frequency dissolved organic carbon and nitrate measurements reveal differences in storm hysteresis and loading in relation to land cover and seasonality, Water Resour. Res., 53, 5345–5363, https://doi.org/10.1002/2017WR020491, 2017.

Wang, J., Li, X., Li, Y., Shi, Y., Xiao, H., Wang, L., Yin, W., Zhu, Z., Bian, H., Li, H., Shi, Z., Seybold, H., and Kirchner, J. W.: Transport pathways of nitrate in stormwater runoff inferred from high-frequency sampling and stable water isotopes, Environ. Sci. Technol., 58, 17026–17035, https://doi.org/10.1021/acs.est.4c02495, 2024.

Yue, F.-J., Li, S.-L., Waldron, S., Oliver, D. M., Chen, X., Li, P., Peng, T., and Liu, C.-Q.: Source availability and hydrological connectivity determined nitrate-discharge relationships during rainfall events in karst catchment as revealed by high-frequency nitrate sensing, Water Res., 231, 119616, https://doi.org/10.1016/j.watres.2023.119616, 2023.

Zhi, W., Li, L., Dong, W., Brown, W., Kaye, J., Steefel, C., and Williams, K. H.: Distinct source water chemistry shapes contrasting concentration–discharge patterns, Water Resour. Res., 55, 4233–4251, https://doi.org/10.1029/2018WR024257, 2019.

Zuecco, G., Penna, D., Borga, M., and van Meerveld, H. J.: A versatile index to characterize hysteresis between hydrological variables at the runoff-event timescale, Hydrol. Process., 30, 1449–1466, https://doi.org/10.1002/hyp.10681, 2016.